

Cite this: *Nanoscale*, 2011, **3**, 4383

www.rsc.org/nanoscale

PAPER

Flow-induced dynamics of carbon nanotubes

Chao Chen and Zhiping Xu*

Received 18th June 2011, Accepted 19th August 2011

DOI: 10.1039/c1nr10641d

The high aspect ratio and bending resilience of a carbon nanotube (CNT) enables it to have remarkable responses to fluid flow. The structural deformation and vibration of a CNT under fluid flow are discussed in this paper, closely tied to their applications in mechanosensing and energy harvesting. We perform molecular dynamics (MD) simulations and a theoretical analysis based on the elastic beam theory, and find that the performance of these applications is critically defined by thermal noise at low flow speeds and flow-induced elastic instabilities at high speeds. We provide a map of operating mechanisms as defined by the properties of both nanostructures and fluid. The results and understanding obtained here could shed some light on the design of nanomechanical devices operating in fluidic environments.

Introduction

In nature, hairy systems consisting of slender fibers are widely utilized by many species as versatile and exceptionally well-adapted mechanotransducers and sensors, including fish, insects, amphibians and human beings. Fluid flow passing hair cells introduces rotating or bending deflections through momentum transfer and interfacial friction forces. These hairy systems exhibit exquisite sensitivity to the local flow environment.^{1–3} For example, human's inner ear hair cell, with cilia that are 2–8 μm tall and 0.1–0.3 μm in diameter, is capable of detecting sound-evoked vibration of nanometres. The cercal wind-receptor hairs of a cricket are between 30 and 1500 μm in length and 1–9 μm in diameter and can detect airflow on the order of 0.01 mm s^{-1} .^{1,2} A typical aspect ratio of these microfibers is on the order of hundreds to thousands.

Understanding the structural deformation and vibration of slender structures as induced by a fluid flow environment is the key to many applications including mechanical energy harvesting and mechanosensing.^{1,2,4,5} Polymer fibers and flexible membranes are utilized for pressure sensors.^{6–11} Piezoelectric slender structures, or artificial 'eels', are placed in the wake of bluff bodies to harvest oscillating mechanical energy from vortices formed in the flow.¹² For a slender fiber cantilevered in a steady shear flow, its deflection under a distributed load is proportional to the fourth order of the aspect ratio α , *i.e.*, $d \sim \alpha^4$. Thus it is promising to take advantage of slender nanofibers with outstanding mechanical properties in mechanosensing applications, such as carbon nanotubes (CNTs), where the aspect ratio can reach as high as

10⁷.¹³ Furthermore, the intrinsic elastic resilience of CNTs and their tubular geometry allow large elastic deformation without material failure.¹⁴ In a previous study, Fakhri *et al.* suggest that single-walled CNTs, as archetypal semi-flexible filaments, are highly suited to act as nano-probes in complex fluids or biological systems.¹⁵ Inorganic piezoelectric nanofibers, such as zinc oxide nanowires, can provide direct conversion from elastic deformation energy into electric polarization and power.^{16,17} Additional merits of these nanofibers include their ultra-high vibrational frequencies providing remarkable sensitivities to high-frequency transient flows. Integrating these novel nanostructures and materials into nanomechanical devices holds great promises of elevating performance in the aforementioned applications.^{18,19}

In order to design novel mechanosensing devices using nanofibers, as inspired by the aforementioned biological hairy systems, here we investigate the structural dynamics of a CNT with distinguished mechanical properties in response to fluid flow. As discussed above, the key features for a nanofiber to establish ultimate flow sensitivities are (1) a high respect ratio α that enables large deflection under a certain flow speed, and (2) excellent elastic resilience that prohibits material failure at large bending deformation or vibration amplitude, and allows a controllable and reversible operating mode. Nanostructures such as CNTs are thus excellent candidates for these applications. However, it is also noticeable that it is very easy for flexible fibers to lose their beam shape and basic vibrational mode in a thermally fluctuating environment. Experimental measurements show that the thermal vibrational amplitude of a 40 nm-long CNT is 0.3 nm.²⁰ Moreover, under high loads tubular nanofibers such as CNTs bear mechanical instabilities, *e.g.*, radial buckling.²¹ These issues leave the applicability and performance of nanofiber based mechanosensing and energy harvesting devices undetermined. The objective of this work is to

Computational Energetics Laboratory (CEL), Department of Engineering Mechanics, School of Aerospace and Center for Nano and Micro Mechanics, Tsinghua University, Beijing, 100084, China. E-mail: xuzp@tsinghua.edu.cn

address these questions. Here we combine molecular dynamics (MD) simulations with a theoretical analysis based on the Euler–Bernoulli beam theory. General design principles for these applications, based on the results, are provided in the discussion that follows.

Materials and methods

As a representative nanofiber system, as shown in Fig. 1(a), we focus on single-walled CNTs and perform MD simulations to capture atomistic processes occurring at the interface between water molecules and the CNT, which govern the interaction and energy transfer between them. In our simulations, we use the large-scale atomic/molecular massively parallel simulator (LAMMPS) package.^{22,23} A capped (5, 5) single-walled CNT of length $L = 5.5$ nm is cantilevered and immersed in a periodic water box with a density of 995.65 kg m^{-3} . The box has dimensions $L_x = 5$ nm, $L_y = 5$ nm in the transverse directions and $L_z = 10$ nm in the z direction, as illustrated in Fig. 1(a). The box size, although larger than the inter-nanotube short-range coupling length, is still not large enough to exclude the long-range hydrodynamic interaction. Thus what we are simulating indeed is an array of CNT with an area density of 0.04 nm^{-2} . In our simulations, one end of the CNT, *i.e.*, two-atom rings, is fixed and all other carbon atoms are set to move according to the interatomic forces on them, following Newtonian equations.

An extended simple point charge (SPC/E) water model is used for the oxygen and hydrogen atoms and intra-molecular interactions in water molecules.²⁴ This model is validated by giving the correct density of water and a dynamic viscosity $\mu = 0.729 \text{ mPa s}$ that is close to the experimental value 0.896 mPa s .²⁵ For the sp^2 bonding between carbon atoms in the CNT we use the Dreiding force field.²⁶ Van der Waals interactions between carbon atoms in the CNT and oxygen atoms in water molecules are described using the Lennard-Jones formula $E_{\text{LJ}} = 4\epsilon[(\sigma/r)^{12} - (\sigma/r)^6]$. This potential function is parameterized as $\epsilon = 4.0626 \text{ meV}$ and $\sigma = 0.319 \text{ nm}$, which corresponds to a contact angle of 95.3 degrees for a water droplet on graphite, consistent with experimental observations.²⁷

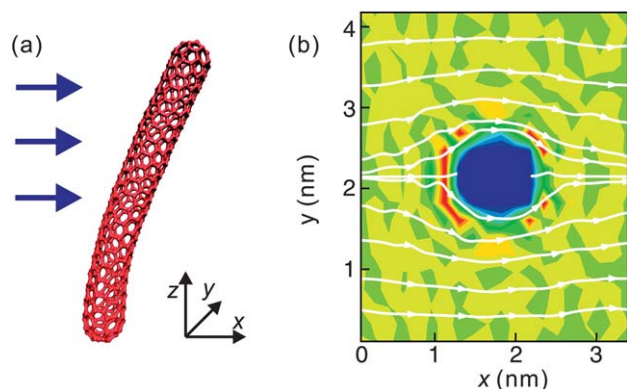


Fig. 1 (a) A schematic illustration of the system in our molecular dynamics (MD) simulations, where a carbon nanotube (CNT) is immersed in a water flow. (b) The flow field of water around the CNT, as viewed in the cross-section plane x - y . The stream lines are represented by arrowed lines and colours map local densities of water.

Our MD simulations are carried out by using a velocity-Verlet algorithm with a time step of 0.5 fs. The SHAKE algorithm is used to apply constraints to oxygen–hydrogen bonds and hydrogen–oxygen–hydrogen angles in water molecules to allow this relatively large time step. The system is first thermalized to 300 K and 1 atm and then maintained for 200 picoseconds in a NVT ensemble, using a N ose–Hoover thermostat to equilibrate water structures and their interfaces with the CNT.

A water flow with velocity v is driven by asserting a constant acceleration in the x -direction on all oxygen atoms in water molecules.²⁸ A N ose–Hoover thermostat is coupled continuously during the flow simulations. In defining the temperature of water molecules, center of mass motion is subtracted from their velocities. The water–CNT system develops into a steady state where the inertial force we apply is balanced by both the flow resistance from the CNT and viscous damping in the fluid. A typical Reynolds number $\text{Re} = \rho Dv/\mu$ here is in the range of 0.01 – 1 as the characteristic length scale is set as $D = 1$ nm. Fig. 1(b) shows the flow field around the CNT, which indicates a distinct creeping flow behaviour.²⁹ As the steady state is reached, usually in hundreds of picoseconds, the deflection curve of CNTs also converges if it is larger than thermally induced fluctuation. The displacement of the CNT tip and its thermally fluctuating amplitude are recorded during the simulations, along with the potential energy stored in the elastic deformation.

Results and discussion

Flow-induced deformation and vibration of a CNT

The displacement amplitudes of the CNT tip in water flow at various Reynolds numbers, or flow velocities are summarized in Fig. 2. We perform MD simulations for both pristine CNTs and those with defects introduced near the fixed end. Results for both of them are plotted in Fig. 2 but effects of defects will be discussed later in the text. When no water flow is driven, the tip position oscillates around its original position $x_0 = x(t=0)$ with a standard deviation of amplitude $a = 0.069$ nm. This thermally induced motion is attributed to both excitations of phonon modes in the CNT and water molecules around it. The averaged bending energy correspondingly is 0.64 eV, which is one order higher than the equipartitioned energy $k_{\text{B}}T = 0.0258$ eV on the first-order vibrational mode. The discrepancy could originate from the finite size effect and high heterogeneity of this system where the energy equipartition cannot be reached. In comparison, we also perform MD simulations in a vacuum for the same CNT, *i.e.*, without water molecules around. The standard deviation of the tip thermal vibration amplitude now is 0.018 nm and the corresponding elastic energy in deformation is 0.44 eV. This result suggests that not only random collisions with surrounding water molecules, but also interaction between the first-order vibration mode and higher order phonon modes lead to elastic distortion to a CNT, which subsequently changes phonon occupation. However, at a much larger length scale, *e.g.*, for a CNT with a length of a few microns, as the frequency difference between low and high order phonon modes increases, the phonon coupling effect is weakened. Thus equipartition theorem can be used to relate thermal vibration amplitude to intrinsic elastic deformation energy of a nanofiber. As examples, thermal

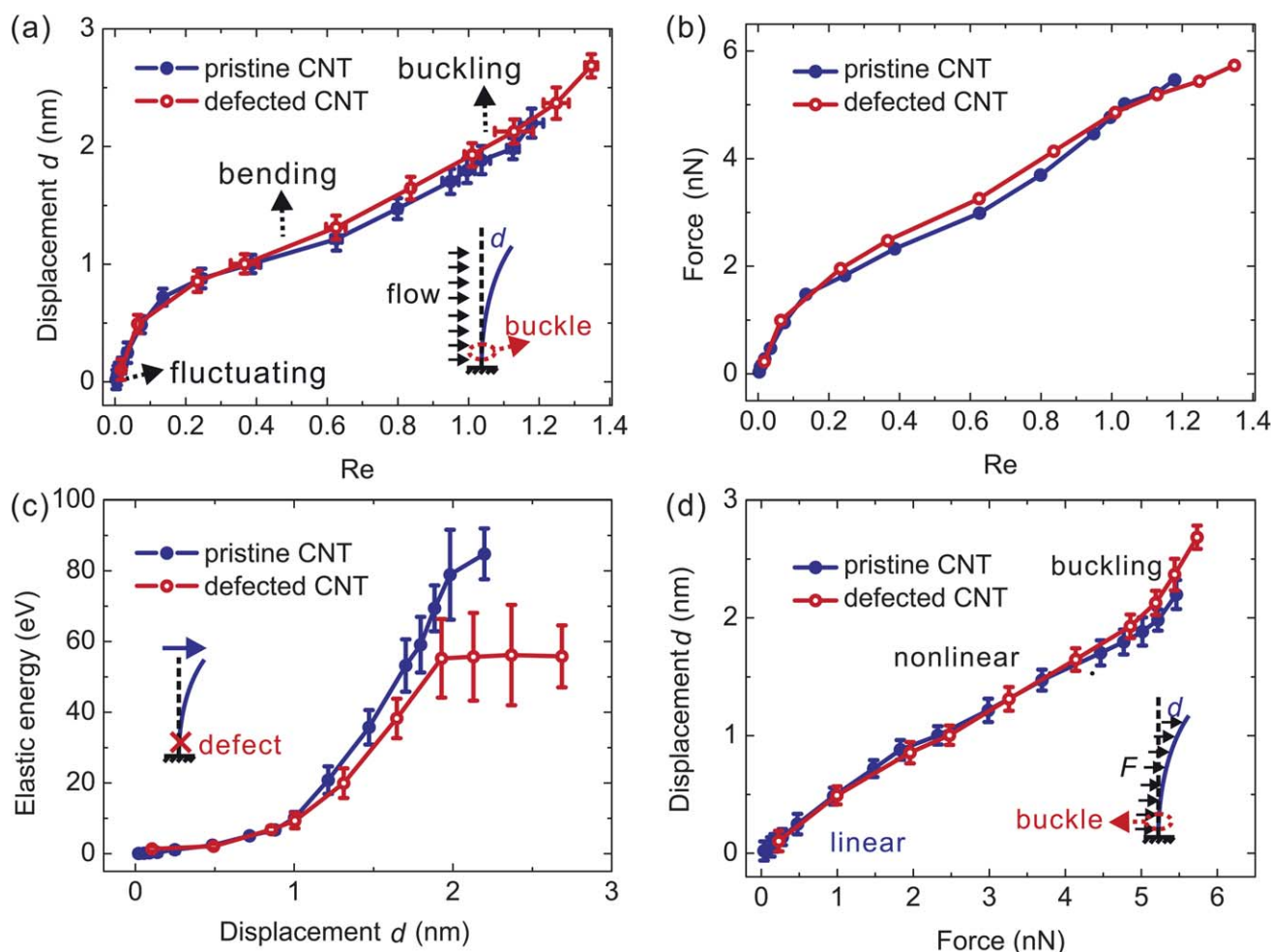


Fig. 2 (a) Tip displacement d and (b) flow-induced force on a (5,5) single-walled CNT at different Reynolds numbers Re (or flow velocities through $Re = \rho Dv/\mu$). (c) The relation between elastic energy stored in a CNT and its tip displacement d under a water flow. The results are plotted for both a pristine CNT (filled circles) and defected CNT with a monatomic vacancy created near the fixed end (open circles, see the inset in subplot (c)). (d) The tip displacement d of a CNT under a uniform load as obtained from an additional MD simulation. Insets in subplots (a) and (d) illustrate the simulation setup for flow-induced bending and uniform load-induced bending of CNTs. Buckles will be formed as the critical Reynolds number Re_b , or stress σ_{cr} is exceeded.

vibration amplitude is successfully applied to estimate Young's modulus and persistence length of a CNT in a vacuum or liquids, which yields reasonable results.^{15,20}

As a water flow is driven at a very low flow speed ($Re < 0.018$), the force felt by the CNT is weaker than that induced by thermal fluctuation. We observe no significant net deflection of the CNT but only random vibration around the equilibrium position x_0 . While at an elevated velocity, for example when $Re = 0.034$, a noticeable first-order deflection mode is observed and the tip of the CNT moves to a new position, denoted as x_v . The tip displacement $d = x_v - x_0$ is plotted in Fig. 2(a). Simulation results show that there is still a thermally driven motion around this new position x_v but the amplitude is reduced because of stiffening of the CNT under bending deformation. The averaged position of the tip x_v moves further at higher flow velocities. The relation between d and Re in Fig. 2(a) shows a linear dependence when $Re < 0.1$ or $d < 0.5$ nm. Beyond this Reynolds number a nonlinear dynamic response of the CNT occurs.

The nonlinearity arises from several origins as follows:

(1) A nonlinear hydrodynamic resistance–Reynolds number relation when Re reaches 0.1 or $d = 0.5$ nm, as shown in Fig. 2(b). We perform additional MD simulations with water flow around a fixed CNT and obtain a resistance–velocity relation. The result shows a dramatic increase of drag force when Re reaches 0.3, which is attributed to the enhancement of fluid–structure coupling.

(2) Nonlinear mechanical properties or constitutive relation of a CNT experiencing bending. Because when both the flow field and CNT deflection reach the steady state simultaneously, local water flow passing each segment of a CNT has the same velocity, so the hydrodynamic drag force applied on the CNT cantilever can be considered as a uniformly distributed load. To investigate the intrinsic response of a CNT to a uniform load applied in the transverse direction, we perform such a MD simulation and obtain a relation between CNT deflection and the total force F applied to it, as plotted in Fig. 2(d). From the simulation results summarized, it is clearly seen that the constitutive relation of a CNT under bending changes from linear to nonlinear and

buckling behaviour as the load increases, as noted in the figure. We find that the tip displacement d keeps a linear relation with the load when d is shorter than 1 nm. Beyond 1 nm, the nonlinear effect shows up. In addition, the elastic buckling of a CNT by local collapse of the cross-section is observed at a much higher load of 5.5 nN (see the insets of Fig. 2(a) and (d)), the corresponding Reynolds number for the water flow is $Re = 1.1$ and the tip displacement of the CNT increases remarkably from 1.98 to 2.20 nm. This sudden jump originates from the onset of a local buckle near the fixed end of the CNT. The change of quadratic energy–deformation tendency in Fig. 2(c) also indicates the buckling phenomenon at $d \sim 1.98$ nm.

(3) A large bending deformation of a cantilevered CNT reduces its effective frontal area to the water flow. This effect is particularly notable as the CNT buckles, where the deflection of a CNT will increase further till orienting horizontally to the substrate. When the tip bends further and points downwards, the CNT segment above the buckle will not feel the load from water flow and thus will be retracted back elastically. The relation between tip displacement and flow velocity thus cannot be determined then due to this instability.

Based on these inspections, the dynamic behaviour of CNTs in water flow can be classified into three regimes, as indicated in Fig. 2(a). Below $Re_{th} = 0.0178$, the structural dynamics of a CNT are dominated by thermal noise, *i.e.*, in the *fluctuating regime*. The deformation and vibration of a CNT in this regime are less correlated with the fluid flow field, and the standard deviation of vibrational amplitude is 0.069 nm at room temperature. Above Re_{th} but below the critical Reynolds number Re_b , corresponds to radial buckling, as we call the elastically *bending regime*, a CNT deflects with a maximal tip displacement $d = 1.98$ nm in the first-order bending mode of an elastic beam. The dynamic behaviour in this regime can be well characterized by the Euler–Bernoulli beam theory. When the Reynolds number of a water flow increases further beyond $Re_b = 1.1$, the CNT buckles. Its cross-section changes from a circle to a flattened shape, and the slope of the displacement–velocity curve increases remarkably.³⁰ We call this the *buckling regime*.

It should be noticed that in our simulations, the velocity range studied (on the order of 10 and 100 m s⁻¹) is relatively large in comparison to the value that a flow sensor or energy harvester usually encounters. The lowest flow velocity in a MD simulation is limited by the size of whole system, *e.g.*, the length of a CNT and water box around. Thus for a short CNT of 5 nm as we investigate here, it needs a much higher flow-induced force to introduce significant deformation. To go beyond this limitation, we develop below a theoretical analysis using Euler–Bernoulli beam theory based on our observation from simulation results, which could be used for a rational design of high-performance mechanosensing and energy harvesting applications.

Transition between fluctuating, bending and buckling mechanisms

Stokes law $C_D \sim Re^{-1}$ in continuum fluid dynamics indicates that for a water flow around a cylinder, the viscous damping coefficient $C_D = F/(S\rho v^2/2)$ is inversely proportional to the Reynolds number for low Re values, where F is the flow resistance, or drag force, and S is the frontal area facing the flow.²⁹ Recent MD

simulations by Walther *et al.* show that although there exists a significant boundary slippage between water molecules and a CNT, the relation between flow resistance and velocity can still be described by Stokes law, as the momentum transfer process that contributes most to the flow resistance is not changed by interfacial slippage.³¹ Our MD simulation results confirm Walther *et al.*'s conclusion and give a scaling law $C_D = C/Re$, where C is 4.467 for a cylinder obstacle in fluid. Using this result and referring to Euler–Bernoulli theory for beam bending, the elastic energy stored in a cantilever beam experiencing a uniform load $q = C\mu v/2$ from fluid flow is calculated as

$$E_b = C^2\mu^2v^2L^5/(160YI), \quad (1)$$

where μ is the dynamic viscosity of fluid, Y is the Young's modulus, I is the second moment of inertia for bending that scales with D^4 for a cylinder with diameter D . At ambient conditions with temperature T , a CNT is in a thermal motion regime with an energy of $k_B T$ distributed to the first-order vibrational mode.²⁰ Applying the equipartition theorem $E_b = k_B T$, we can define the critical thermal flow velocity as

$$v_{th} = \frac{4}{C\mu L^2} \sqrt{\frac{10k_B T Y I}{L}}. \quad (2)$$

Beyond this velocity, the structural dynamics of a CNT makes a transition from thermal vibration to a static deflection. The amplitude is determined by the flow-induced force. The prediction from eqn (2) is not adequate for finite and heterogeneous systems as discussed before, but for CNTs with a larger length and diameter where equipartition theorem holds, eqn (2) should yield correct results.

Furthermore, by assuming the hydrodynamic force is uniformly applied on the CNT, the tip deflection d is calculated as

$$d = 3C\mu v_{th} L^4/(48YI), \quad (3)$$

which scales with L^4 . As $I = \pi D^4/64$ for circular cross-sections, d is then proportional to α^4 , where $\alpha = L/D$ is the aspect ratio. This relation implies that nanofibers with ultra-high α values have a remarkable response to low speed flows. At increasing flow velocities, a single-walled CNT buckles by forming a locally flattened cross-section. With the critical stress σ_{cr} defined for the onset of this instability, the buckling regime thus starts from a critical velocity

$$v_b = 8\sigma_{cr} I/(C\mu L^2 D) \quad (4)$$

The deflection of a CNT experiencing a uniformly distributed load is plotted in Fig. 2(d). It can be seen that as buckling or rippling occurs, the displacement–force relation has a double-linear shape.³² The bending stiffness $D_b = YI$ is significantly lowered as the buckling occurs, and the buckle point acts similarly as a hinge, allowing much magnified tip displacement. According to ref. 30, the buckling load can be predicted as $\sigma_{cr} = 45$ GPa. The critical Reynolds number $Re_b = 0.8$ is consistent with our MD simulation results.

The buckling mechanism observed in our simulations offers a protective solution against materials failure at high loads and extends the working range for the flow velocities. Furthermore,

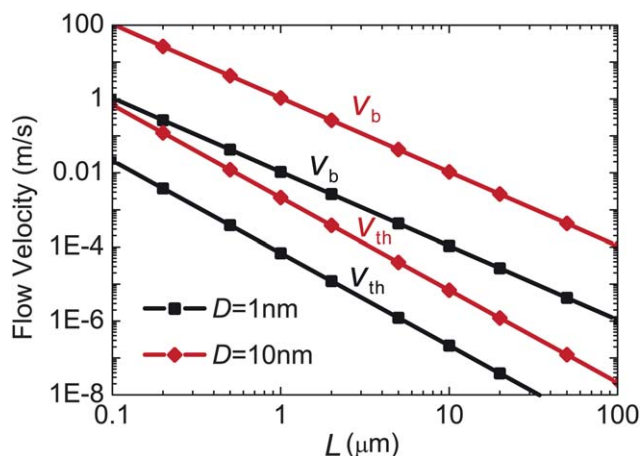


Fig. 3 Critical flow velocities v_{th} and v_b of a water flow around a CNT with specific geometric properties (diameter D and length L), corresponding to the transitions from fluctuating to bending, and buckling regimes respectively.

as after the CNT buckles, its bending stiffness is significantly lowered, flow sensors working in the buckling regime thus have a larger response to the flow field. For multi-walled CNTs, delocalized rippling, instead of local buckling, is observed under a bending load. It is also reported that the bending stiffness is lowered after rippling and similar effects on the relation between flow velocity and deflection amplitude are expected.^{21,32,33}

Further engineering on the structure of a CNT, for example, by introducing defects near its fixed end, could be pursued to reduce critical stress σ_{cr} and allow a CNT to buckle at a smaller load. This will extend the operating flow speed range in the buckling regime. For verification, we perform additional MD simulations by creating a monatomic vacancy or a Stone–Wales dislocation at the position right above the fixed carbon atoms. The monatomic vacancy shows a more marked effect. The tip displacement plotted in Fig. 2(a) and (d) shows enhanced amplitudes at high flow speeds or uniform loads after a defect is introduced, especially after transition into the buckling regime. On the other hand, as the bending rigidity is reduced by this imperfection, the corresponding elastic energy stored in the CNT decreases, as shown in Fig. 2(c). In experimental implementations, CNTs are usually mounted on a surface, where translational and rotational flexibilities at the contact could act as a pivot. Rotation in addition to bending could also be induced by the flow. Actually, many biological mechanosensing systems as introduced earlier in the text follow this mechanism.³⁴

Conclusion

Based on the results obtained above, we conclude that the bottom limit of using nanofibers such as CNTs for mechanosensing and energy harvesting applications is defined by the competition between flow-induced elastic deformation and fluctuation from thermal noises. The quantitative prediction of v_{th} and v_b are provided in Fig. 3, showing that for a typical CNT with a diameter of 1 nm and a length of 1 μm , the maximum sensitivity can reach 68 $\mu\text{m s}^{-1}$ when it is immersed in water, which is of great interest when compared with available commercial flow sensors.

To establish such an application, there are still some practical issues to be solved beyond the scope of this paper. For a long CNT, thermal fluctuations and energy coupling between different vibrational modes could excite its second or higher-order vibrational modes. In this situation, the analytical model presented previously should be improved to include higher-order effects. To magnify the readouts from flow-induced bending motion, a scalable approach is to pattern CNTs or CNT fibers in an array. In these systems, inter-fiber communication as mediated by hydrodynamic interactions will result in interference or synchronization between the bending motion of neighbouring fibers, which requires further exploration.³ When the CNTs are mounted on a substrate, the flow field adjacent to its surface will differ from the center of a flow channel as boundary slippage occurs there. The flow speed distribution along the CNT at that region, as determined by the substrate material properties and surface microstructures, need also to be identified to predict the performance of mechanosensing.

It is also straightforward to extend our analysis to other nanofibers including inorganic nanowires, or more interestingly, fibrous and tubular proteins and cytoskeleton networks to study the effects of flow on their biological functions.^{35–37} Other fluid environments can also be treated, such as air, where a free-molecule flow model should be used to estimate atmospheric pressure instead of the creeping flow theory applied here.^{38,39}

Acknowledgements

This work is supported by Tsinghua University through the Key Talent Support Program and the National Science Foundation of China through Young Scholar Grant 11002079. This work is also supported by Shanghai Supercomputer Center of China.

References

- 1 P. Fratzl and F. G. Barth, *Nature*, 2009, **462**, 442–448.
- 2 M. E. McConney, K. D. Anderson, L. L. Brott, R. R. Naik and V. V. Tsukruk, *Adv. Funct. Mater.*, 2009, **19**, 2527–2544.
- 3 A. S. Kozlov, J. Baumgart, T. Risler, C. P. C. Versteegh and A. J. Hudspeth, *Nature*, 2011, **474**, 376–379.
- 4 X. Chen, S. Xu, N. Yao and Y. Shi, *Nano Lett.*, 2010, **10**, 2133–2137.
- 5 K. Jensen, K. Kim and A. Zettl, *Nat. Nanotechnol.*, 2008, **3**, 533–537.
- 6 G. J. M. Krijnen, M. Dijkstra, J. J. van Baar, S. S. Shankar, W. J. Kuipers, R. J. H. de Boer, D. Altpeter, T. S. J. Lammerink and R. Wiegink, *Nanotechnology*, 2006, **17**, S84–S89.
- 7 C. Liu, *Bioinspir. Biomimetics*, 2007, **2**, S162–S169.
- 8 N. C. Tucker, C. Engel, Y. Y. Pandya and C. Liu, *J. Microelectromech. Syst.*, 2007, **16**, 999–1014.
- 9 S. C. B. Mannsfeld, B. C. K. Tee, R. M. Stoltenberg, C. V. H. H. Chen, S. Barman, B. V. O. Muir, A. N. Sokolov, C. Reese and Z. Bao, *Nat. Mater.*, 2010, **9**, 859–864.
- 10 M. E. McConney, N. Chen, D. Lu, H. A. Hu, S. Coombs, C. Liu and V. V. Tsukruk, *Soft Matter*, 2009, **5**, 292–295.
- 11 S. A. Sarles, J. D. W. Madden and D. J. Leo, *Soft Matter*, 2011, **7**, 4644–4653.
- 12 J. J. Allen and A. J. Smits, *J. Fluids Struct.*, 2001, **15**, 629–640.
- 13 Q. Wen, W. Qian, J. Nie, A. Cao, G. Ning, Y. Wang, L. Hu, Q. Zhang, J. Huang and F. Wei, *Adv. Mater.*, 2010, **22**, 1867–1871.
- 14 M. S. Dresselhaus, G. Dresselhaus and P. Avouris, *Carbon nanotubes: synthesis, structure, properties and applications*, Springer, New York, 2000.
- 15 N. Fakhri, D. A. Tsybolski, L. Cognet, R. B. Weisman and M. Pasquali, *Proc. Natl. Acad. Sci. U. S. A.*, 2009, **106**, 14219–14223.
- 16 Z. L. Wang and J. Song, *Science*, 2006, **312**, 242–246.
- 17 Y. H. Yang, Y. Zhang, N. W. Wang, C. X. Wang, B. J. Li and G. W. Yang, *Nanoscale*, 2011, **3**, 592–597.

- 18 K. Eom, H. S. Park, D. S. Yoon and T. Kwon, *Phys. Rep.*, 2011, **503**, 115–163.
- 19 J. L. Arlett, E. B. Myers and M. L. Roukes, *Nat. Nanotechnol.*, 2011, **6**, 203–215.
- 20 M. M. J. Treacy, A. Krishnan and P. N. Yianilos, *Microscopy and Microanalysis*, 2000, **6**, 317–323.
- 21 M. R. Falvo, G. J. Clary, R. M. Taylor, V. Chi, F. P. Brooks, S. Washburn and R. Superfine, *Nature*, 1997, **389**, 582–584.
- 22 S. Plimpton, *J. Comput. Phys.*, 1995, **117**, 1–19.
- 23 C. Chen, M. Ma, Z. Liu, Q. Zheng and Z. Xu, *J. Appl. Phys.*, 2011, **110**, 034320.
- 24 H. J. C. Berendsen, J. R. Grigera and T. P. Straatsma, *J. Phys. Chem.*, 1987, **91**, 6269–6271.
- 25 M. A. Gonzalez and J. L. F. Abascal, *J. Chem. Phys.*, 2010, **132**, 096101.
- 26 Y. Guo, N. Karasawa and W. A. Goddard, *Nature*, 1991, **351**, 464–467.
- 27 D. Mattia and Y. Gogotsi, *Microfluid. Nanofluid.*, 2008, **5**, 289–305.
- 28 X. Chen, G. Cao, A. Han, V. K. Punyamurtula, L. Liu, P. J. Culligan, T. Kim and Y. Qiao, *Nano Lett.*, 2008, **8**, 2988–2992.
- 29 J. Happel and H. Brenner, *Low Reynolds number hydrodynamics*, Martinus Nijhoff Publishers, The Hague, 1983.
- 30 G. Cao and X. Chen, *Phys. Rev. B: Condens. Matter Mater. Phys.*, 2006, **73**, 155435.
- 31 J. H. Walther, T. Werder, R. L. Jaffe and P. Koumoutsakos, *Phys. Rev. E: Stat., Nonlinear, Soft Matter Phys.*, 2004, **69**, 062201.
- 32 J. Z. Liu, Q. Zheng and Q. Jiang, *Phys. Rev. Lett.*, 2001, **86**, 4843–4847.
- 33 X. Q. He, S. Kitipornchai and K. M. Liew, *J. Mech. Phys. Solids*, 2005, **53**, 303–326.
- 34 F. G. Barth, *Naturwissenschaften*, 2000, **87**, 51–58.
- 35 S. Keten, Z. Xu, B. Ihle and M. J. Buehler, *Nat. Mater.*, 2010, **9**, 359–367.
- 36 Z. Xu, R. Paparcone and M. J. Buehler, *Biophys. J.*, 2010, **98**, 2053–2062.
- 37 S. Keten, J. Rodriguez Alvarado, S. Müftü and M. Buehler, *Cell. Mol. Bioeng.*, 2009, **2**, 66–74.
- 38 M. J. Martin and B. H. Houston, *Appl. Phys. Lett.*, 2007, **91**, 103116.
- 39 S. S. Verbridge, R. Ilic, H. G. Craighead and J. M. Parpia, *Appl. Phys. Lett.*, 2008, **93**, 013101.